1 **Inter-comparison and improvement of two-stream shortwave radiative transfer**
2 **models for a unified treatment of cryospheric surfaces in ESMs**
3

4 Cheng Dang[1], Charles S. Zender[1], Mark G. Flanner[2]
5
6 [1] Department of Earth System Science, University of California, Irvine, CA, USA
7 [2] Department of Climate and Space Sciences and Engineering, University of Michigan,
8 Ann Arbor, MI, USA
9 *Correspondence to*: Cheng Dang (cdang5@uci.edu)

10

11 **Abstract.** Snow is an important climate regulator because it greatly increases the surface
12 albedo of large parts of the Earth. Earth System Models (ESMs) often adopt two-stream
13 approximations with different radiative transfer techniques, the same snow therefore has
14 different solar radiative properties depending on whether it is on land or on sea ice. Here
15 we inter-compare three two-stream algorithms widely used in snow models, improve
16 their predictions at large zenith angles, and introduce a hybrid model suitable for all
17 cryospheric surfaces in ESMs. The algorithms are those employed by the SNow ICe and
18 Aerosol Radiative (SNICAR) module used in land models, and by dEdd-AD used in
19 Icepack, the column physics used in the Los Alamos sea ice model CICE and MPAS-
20 seaice, and a two-stream discrete ordinate (2SD) model. Compared with a 16-stream
21 benchmark model, the errors in snow visible albedo for a direct-incident beam from all
22 three two-stream models are small ($<\pm0.005$) and increase as snow shallows, especially
23 for aged snow. The errors in direct near-infrared (near-IR) albedo are small ($<\pm0.005$) for
24 solar zenith angles $\theta < 75°$, and increase as θ increases. For diffuse incidence under
25 cloudy skies, dEdd-AD produces the most accurate snow albedo for both visible and
26 near-IR ($<\pm0.0002$) with the lowest underestimate (-0.01) for melting thin snow.
27 SNICAR performs similarly to dEdd-AD for visible albedos, with a slightly larger
28 underestimate (-0.02), while it overestimates the near-IR albedo by an order of magnitude
29 more (up to 0.04). 2SD overestimates both visible and near-IR albedo by up to 0.03. We
30 develop a new parameterization that adjusts the underestimated direct near-IR albedo and
31 overestimated direct near-IR heating persistent across all two-stream models for solar
32 zenith angles $> 75°$. These results are incorporated in a hybrid model SNICAR-AD,
33 which can now serve as a unified solar radiative transfer model for snow in ESM land,
34 land ice, and sea-ice components.

35

Author
Deleted: Icepack
Author
Deleted: Icepack

1. Introduction

Snow cover on land, land ice, and sea ice, modulates the surface energy balance of mid and high latitudes of the Earth, principally because even a thin layer of snow can greatly increase the surface albedo. Integrated over the solar spectrum, the broadband albedo of opaque snow ranges from 0.7 – 0.9 (e.g., Wiscombe and Warren 1980; Dang et al., 2015). In contrast, the albedo of other natural surfaces is smaller: 0.2, 0.25, and 0.5-0.7 for damp soil, grassland, and bare multi-year sea ice, respectively (Perovich 1996; Liang et al., 2002; Brandt et al., 2005; Bøggild et al., 2010). The accumulation, evolution, and depletion of snow cover modify the seasonal cycle of surface albedo globally. In particular, snow over sea ice absorbs more solar energy and begins to melt in the spring, which forms melt ponds that bring the sea-ice albedo to as low as 0.15 to further accelerate ice melt (Light et al., 2008, 2015). An accurate simulation of the shortwave radiative properties of snowpack is therefore crucial for spectrally partitioning solar energy and representing snow-albedo feedbacks across the Earth system. Unfortunately, computational demands and coupling architectures often constrain representation of snowpack radiative processes in Earth System Models (ESMs, please refer to Table 1 for all acronyms used in this work) to relatively crude approximations such as two-stream methods (Wiscombe and Warren, 1980, Toon et al., 1989). In this work, we inter-compare two-stream methods widely used in snow models and then introduce a new parameterization that significantly reduces their snowpack reflectance and heating biases at large zenith angles, to produce more realistic behavior in polar regions.

Snow albedo is determined by many factors including the snow grain radius, the solar zenith angle, cloud transmittance, light-absorbing particles, and the albedo of underlying ground if snow is optically thin (Wiscombe and Warren, 1980; Warren and Wiscombe, 1980); it also varies strongly with wavelength since the ice absorption coefficient varies by 7 orders of magnitudes across the solar spectrum (Warren and Brandt, 2008). At visible wavelengths (0.2 - 0.7 μm), ice is almost non-absorptive such that the absorption of visible energy by snowpack is mostly due to the light-absorbing particles (e.g. black carbon, organic carbon, mineral dust) that were incorporated during ice nucleation in clouds, scavenged during precipitation, or slowly sedimented from the atmosphere by gravity (Warren and Wiscombe, 1980, 1985; Doherty et al., 2010, 2014, 2016; Wang et al., 2013; Dang and Hegg 2014). As snow becomes shallower, visible photons are more likely to penetrate through snowpack and get absorbed by darker underlying ground. At near-infrared (near-IR) wavelengths (0.7 – 5 μm), ice is much more absorptive that the

snow albedo is lower than the visible albedo. Larger ice crystals form a lower albedo surface than smaller ice crystals hence aged snowpacks absorb more solar energy. Photons incident at smaller solar zenith angles are more likely to penetrate deeper vertically and be scattered in the snowpack until being absorbed by the ice/the underlying ground/absorbing impurities, which also leads to a smaller snow albedo. To compute the reflected solar flux, spectrally resolved albedo must be weighted by the incident solar flux, which is mostly determined by solar zenith angle, cloud cover and transmittance, and column water vapor. Modeling the solar properties of snowpacks must consider the spectral signatures of these atmospheric properties.

Several parameterizations have been developed to compute the snow solar properties without solving the radiative transfer equations and some are incorporated into ESMs or regional models. Marshall and Warren (1987) and Marshall (1989) parameterized snow albedo in both visible and near-IR bands as functions of snow grain size, solar zenith angle, cloud transmittance, snow depth, underlying surface albedo, and black carbon content. Marshall and Oglesby (1994) used this in an ESM. Gardner and Sharp (2010) parameterized the all-wave snow albedo with similar inputs. This was incorporated into the regional climate model RACMO (https://www.projects.science.uu.nl/iceclimate/models/racmo.php) to simulate snow albedo in glaciered regions like Antarctica and Greenland (Munneke et al., 2011). Dang et al., (2015) compute snow albedo as functions of snow grain radius, black carbon content, and dust content for visible and near-IR bands and 14 narrower bands used in the rapid radiative transfer model (RRTM, Mlawer and Clough, 1997). Their parameterization can also be expanded to different solar zenith angles using the zenith angle parameterization developed by Marshall and Warren (1987). Aoki et al., (2011) developed a more complex model based on the offline snow albedo and a transmittance look-up table. This can be applied to multilayer snowpack to compute the snow albedo and the solar heating profiles as functions of snow grain size, black carbon and dust content, snow temperature, and snowmelt water equivalent. These parameterizations are often in the form of simplified polynomial equations, which are especially suitable to long-term ESM simulations that require less time-consuming snow representations.

More complex models that explicitly solve the multiple scattering radiative transfer equations have also been developed to compute snow solar properties. Flanner and Zender (2005) developed the SNow Ice and Aerosol Radiation model (SNICAR) that utilizes two-stream approximations (Wiscombe and Warren 1980; Toon et al., 1989) to

predict heating and reflectance for multi-layer snowpack. They implemented SNICAR in the Community Land Model (CLM) to predict snow albedo and vertically-resolved solar absorption for snow-covered surfaces. Before SNICAR, CLM prescribed snow albedo and confined all solar absorption to the top snow layer (Flanner and Zender 2005). Over the past decades, updates and new features have been added to SNICAR to consider more processes such as black carbon/ice mixing states (Flanner et al., 2012) and snow grain shape (He et al., 2018b). Concurrent with the development of SNICAR, Briegleb and Light (2007) improved the treatment of sea-ice solar radiative calculations in Community Climate System Model (CCSM). They implemented a different two-stream scheme with delta-Eddington approximation and adding-doubling technique (hereafter, dEdd-AD) that allows CCSM to compute bare/ponded/snow-covered sea ice albedo and solar absorption profiles of multi-layer sea ice. Before these improvements, the sea-ice albedo was computed based on surface temperature, snow thickness, and sea-ice thickness using averaged sea ice and snow albedo. dEdd-AD has been adopted by the sea-ice physics library Icepack (https://github.com/CICE-Consortium/Icepack/wiki), which is used by the Los Almos Sea Ice Model CICE (Hunke et al., 2010) and Model for Prediction Across Scales Sea Ice MPAS-seaice (Turner et al., 2018). CICE itself is used in numerous global and regional models.

SNICAR and dEdd-AD solve the multiple scattering radiative transfer equations and provide much improved solar radiative representations for the cryosphere, though their separate development and implementation created an artificial divide for snow simulation. In ESMs that utilize both SNICAR and dEdd-AD, such as the Community Earth System Model (CESM, http://www.cesm.ucar.edu/) and the Energy Exscale Earth System Model (E3SM, previously known as ACME, https://e3sm.org/), the solar radiative properties of snow on land and snow on sea ice are computed separately via SNICAR and dEdd-AD. As a result, the same snow in nature has different solar radiative properties such as reflectance depending on which model represents it. These differences are model artifacts that should be eliminated so that snow has consistent properties across the Earth system.

In this paper, we evaluate the accuracy and biases of three two-stream models listed in Table 2, including the algorithms used in SNICAR and dEdd-AD, at representing reflectance and heating. In Sections 2-4, we describe the radiative transfer algorithms and calculations performed in this work. The results and model inter-comparisons are discussed in Section 5. In Section 6, we introduce a parameterization to reduce the

4

165 simulated albedo and heating bias for solar zenith angles larger than 75°. In Section 7, we
166 summarize the major differences of algorithm implementations between SNICAR and
167 dEdd-AD in ESMs. We use these results to develop and justify a unified surface
168 shortwave radiative transfer method for all Earth system model components in the
169 cryosphere, presented in Section 8.

170

2. Radiative Transfer Model

171
172
173 In this section, we summarize the three two-stream models and the benchmark DISORT
174 model with 16-streams. These algorithms are well documented in papers by Toon et al.,
175 (1989), Briegleb and Light (2007), Jin and Stamnes (1994), and Stamnes et al. (1988).
176 Readers interested in detailed mathematical derivations should refer to those papers. We
177 only include their key equations to illustrate the difference among two-stream models for
178 discussion purposes.

179
180 2.1 SNICAR in land models CLM and ELM
181 SNICAR is implemented as the default snow shortwave radiative transfer scheme in
182 CLM and E3SM land model (ELM). It adopts the two-stream algorithms and the rapid
183 solver developed by Toon et al., (1989) to compute the solar properties of multi-layer
184 snowpacks. These two-stream algorithms are derived from the general equation of
185 radiative transfer in a plane parallel media:

186

187 $$\mu \frac{\partial I}{\partial \tau}(\tau, \mu, \Phi) = I(\tau, \mu, \Phi) - \frac{\varpi}{4\pi} \int_0^{2\pi} \int_{-1}^{1} P(\mu, \mu', \phi, \phi') I(\tau, \mu', \Phi') d\mu' d\phi' - S(\tau, \mu, \Phi)$$

188
189 (1)
190
191
192 where arccos(μ) and Φ are zenith angle and azimuth angle, ϖ is single-scattering albedo.
193 On the right-hand side, the three terms are intensity at optical depth τ, internal source
194 term due to multiple scattering, and external source term S. For a purely external source
195 at solar wavelengths S is:

196

197 $$S = \frac{\varpi}{4} F_s P(\mu, -\mu_0, \phi, \phi_0) exp\left(\frac{-\tau}{\mu_0}\right)$$ (2)

198

199 where πF_s is incident solar flux, μ_0 is the incident direction of the solar beam. Integrating
200 equation (1) over azimuth and zenith angles yields the general solution of two-stream

Author
Deleted: .

202 approximations (Meador and Weaver, 1980). The upward and downward fluxes at optical
203 depth τ of layer n can be represented as:

206 $$F_n^+ = k_{1n} \, exp(\Lambda_n \tau) + \Gamma_n k_{2n} \, exp(-\Lambda_n \tau) + C_n^+(\tau) \qquad (3a)$$

208 $$F_n^- = \Gamma_n k_{1n} \, exp(\Lambda_n \tau) + k_{2n} \, exp(-\Lambda_n \tau) + C_n^-(\tau) \qquad (3b)$$

211 where Λ_n, Γ_n C_n are known coefficients determined by the two-stream method, incident
212 solar flux, and solar zenith angle; whereas k_{1n} and k_{2n} are unknown coefficients
213 determined by the boundary conditions. For an N-layer snowpack, the solutions for
214 upward and downward fluxes are coupled at layer interfaces to generate 2N equations
215 with 2N unknown coefficients k_{1n} and k_{2n}. Combining these equations linearly generates
216 a new set of equations with terms in tridiagonal form that enables the application of a fast
217 tri-diagonal matrix solver. With the solved coefficients, the upward and downward fluxes
218 are computed at different optical depths (Equations 3a and 3b) and eventually the
219 reflectance, transmittance, and absorption profiles of solar flux for any multilayer
220 snowpack.

222 SNICAR itself implements all three two-stream algorithms in Toon et al., (1989):
223 Eddington, Quadrature, and Hemispheric-mean. In practical simulations, it utilizes the
224 Eddington and Hemispheric-mean approximations to compute the visible and near-IR
225 snow properties, respectively (Flanner et al., 2007). In addition to their algorithms,
226 SNICAR implements the Delta-transform of the fundamental input variables asymmetry
227 factor (g), single-scattering albedo (ϖ), and optical depth (τ) to account for the strong
228 forward scattering in snow (Equations 2 (a)-(c), Wiscombe and Warren, 1980).

230 2.2. dEdd-AD in sea ice models Icepack, CICE, and MPAS-seaice
231 Icepack, CICE, and MPAS-seaice use the same shortwave radiative scheme dEdd-AD
232 developed and documented by Briegleb and Light (2007). Sea ice is divided into multiple
233 layers to first compute the single-layer reflectance and transmittance using two-stream
234 delta-Eddington solutions to account for the multiple scattering of light within each layer
235 (Equation set 50, Briegleb and Light, 2007), where the name "delta" implies dEdd-AD
236 implements the Delta-transform to account for the strong forward scattering of snow and

Author
Deleted: solar

Author
Deleted: treatment

Author
Deleted: In the following discussions, we will refer to this method as CICE since it is more widely used.

Author
Deleted:), where

Author
Deleted: the

Author
Deleted: CICE

sea ice (Equations 2 (a)-(c), Wiscombe and Warren, 1980). The single-layer direct albedo and transmittance are computed by equations:

$$R(\mu_{0,n}) = A_n\, exp\left(\frac{-\tau}{\mu_{0,n}}\right) + B_n(exp(\varepsilon_n \tau) - exp(-\varepsilon_n \tau)) - K_n \tag{4a}$$

$$T(\mu_{0,n}) = E_n + H_n(exp(\varepsilon_n \tau) - exp(-\varepsilon_n \tau))\, exp\left(\frac{-\tau}{\mu_{0,n}}\right) \tag{4b}$$

where coefficients A_n, B_n, K_n, E_n, H_n, and ε_n are determined by the single-scattering albedo (ϖ), asymmetry factor (g), optical depth (τ), and angle of the incident beam at layer n ($\mu_{0,n}$). Following the delta-Eddington assumption, simple formulas are available for the single-layer reflectance and transmittance under both clear sky (direct flux, equations 4a and 4b) and overcast sky (diffuse flux) conditions, however, the formula derived by applying diffuse-flux upper boundary conditions sometimes yields negative albedos (Wiscombe 1977). To avoid the unphysical values, diffuse reflectance $\bar{R}$ and transmittance $\bar{T}$ of a single layer are computed by integrating the direct reflectance $R(\mu)$ and transmittance $T(\mu)$ over the incident hemisphere assuming isotropic incidence:

$$\bar{R} = 2 \int_0^1 \mu R(\mu) d\mu \tag{5a}$$

$$\bar{T} = 2 \int_0^1 \mu T(\mu) d\mu \tag{5b}$$

This is the same as the method proposed by Wiscombe and Warren (1980, their equation 5). In practice, eight Gaussian angles are implemented to perform the integration for every layer.

The computed single-layer reflectance and transmittance of direct and diffuse components are then combined to account for the inter-layer scattering of light to compute the reflectance and transmission at every interface (Equation set 51, Briegleb and Light, 2007), and eventually the upward and downward fluxes (Equation set 52, Briegleb and Light, 2007). These upward and downward fluxes at each optical depth are then used to compute the column reflectance and transmittance, and the absorption profiles for any multilayered media, such as snowpacks on land and sea ice.

In nature, a large fraction of sea ice is covered by snow during winter. As snow melts away in late spring and summer, it exposes bare ice, and melt ponds form on the ice

Author
Deleted: se

7

surface. Such variation of sea-ice surface types requires the shortwave radiative transfer model to be flexible and capable of capturing the light refraction and reflection. Refractive boundaries exist where air (refractive index $m_{re} = 1.0$), snow (assuming snow as medium of air containing a collection of ice particles, $m_{re} = 1.0$), pond (assuming pure water, $m_{re} = 1.33$), and ice (assuming pure ice, $m_{re} = 1.31$) are present in the same sea-ice column. The general solution of delta-Eddington, and the two-stream algorithms used in SNICAR are not applicable to such non-uniformly refractive layered media. To include the effects of refraction, Briegleb and Light (2007) modified the adding formula at the refractive boundaries (i.e. interfaces between air/ice, snow/ice, air/pond). The reflectance and transmittance of the adjacent layers above and below the refractive boundary are combined with modifications to include the Fresnel reflection and refraction of direct and diffuse fluxes (Section 4.1, Briegleb and Light, 2007). dEdd-AD can thus be applied to any layered media with either uniform (e.g., snow on land) or non-uniform (e.g., snow on sea ice) refractive indexes.

In this paper, we apply dEdd-AD to snowpacks that can be treated as uniform refractive media such as the air/snowpack/land columns assumed in SNICAR for model evaluation. An ideal radiative treatment for snow should, however, keep the potential to include refraction for further applications to snow on sea ice or ice sheets. Therefore, besides these two widely used algorithms in Icepack and SNICAR, we evaluate a third algorithm (section 2.3) that can be applied to layered media with either uniform or non-uniform refractive indexes.

2.3. two-stream discrete-ordinate algorithm (2SD)

A refractive boundary also exists between the atmosphere and the ocean, and models have been developed to solve the radiative transfer problems in the atmosphere-ocean system using the discrete-ordinate technique (e.g. Jin and Stamnes, 1994; Lee and Liou, 2007). Similar to the two-stream algorithms of Toon et al., (1989) used in SNICAR, Jin and Stamnes (1994) also developed their algorithm from the general equation:

$$\mu \frac{\partial I}{\partial \tau}(\tau, \mu) = I(\tau, \mu) - \frac{\varpi}{4\pi} \int_{-1}^{1} P(\tau, \mu, \mu') I(\tau, \mu') d\mu' - S(\tau, \mu) \qquad (6)$$

Equation (6) is the azimuthally integrated version of equation (1). However, for vertically inhomogeneous media like the atmosphere-ocean or sea ice, the external source term $S(\tau, \mu)$ is different. Specifically, for the medium of total optical depth τ^a above the

Author
Deleted: This adding-doubling delta-Eddington method

Author
Deleted: .

Author
Deleted: focus on

refractive interface, one must consider the contribution from the upward beam reflected at the refractive boundary (second term on the right-hand side):

$$S^a(\tau,\mu) = \frac{\varpi}{4\pi} F_s P(\tau,-\mu_0,\mu) \, exp\left(\frac{-\tau}{\mu_0}\right) + \frac{\varpi}{4\pi} F_s R(-\mu_0,m) P(\tau,+\mu_0,\mu) exp\left(\frac{-(2\tau^a-\tau)}{\mu_0}\right)$$

$$(7)$$

where $R(-\mu_0,m)$ is the Fresnel reflectance of radiation and m is the ratio of the refractive indices of the lower to the upper medium. For the medium below the refractive interface, one must account for the Fresnel transmittance $T(-\mu_0,m)$ and modify the angle of beam travel in media b:

$$S^b(\tau,\mu) = \frac{\varpi}{4\pi} \frac{\mu_0}{\mu_{0n}} F_s T(-\mu_0,m) P(\tau,-\mu_0,\mu) \, exp\left(\frac{-\tau^a}{\mu_0}\right) exp\left(\frac{-(\tau-\tau^a)}{\mu_{0n}}\right) \qquad (8)$$

where μ_{0n} is the cosine zenith angle of refracted beam incident at angle μ_0 above the refractive boundary, by Snell's law:

$$\mu_{0n} = \sqrt{1-(1-\mu_0^2)/m^2} \qquad (9)$$

For uniformly refractive media like snow on land, one can just set the refractive index m_{re} equal to 1 for every layer. In this case, the Fresnel reflectance $R(-\mu_0,m)$ is 0 in equation (7), the Fresenal transmittance $T(-\mu_0,m)$ is 1 in equation (8), and μ_{0n} equals to μ_0: the two source terms $S^a(\tau,\mu)$ and $S^b(\tau,\mu)$ become the same and equal to the source term of homogenous media given in equation (2).

For two-stream approximations of this method, analytical solutions of upward and downward fluxes are coupled at each layer interface to generate 2N equations with 2N unknown coefficients for any N-layer stratified column. The solutions of two-stream algorithms and boundary conditions for homogenous media are well documented (Sections 8.4 and 8.10 of Thomas and Stamnes, 1999). Despite the extra source terms, these 2N equations can also be organized into a tridiagonal matrix similar to the method of Toon et al. (1989) used in SNICAR. Flexibility and speed therefore make this two-stream discrete-ordinate algorithm (hereafter, 2SD) a potentially good candidate for long-

9

353 term Earth system modeling. In this work, we only apply 2SD to snowpack and note that
354 it can be applied to any uniformly or non-uniformly refractive media like snow on land or
355 sea ice, with the Delta-transform implemented to fundamental optical variables
356 (Equations 2 (a)-(c), Wiscombe and Warren, 1980).

357

358 2.4 16-stream DISORT
359 Besides the mathematical technique, the accuracy and speed of radiative transfer
360 algorithms depend on the number of angles used for flux estimation in the upward and
361 downward hemispheres. SNICAR, dEdd-AD, and 2SD use one angle to represent upward
362 flux and one angle to represent downward flux, hence they are named two-stream
363 algorithm. Lee and Liou (2007) use two upward and two downward streams. Jin and
364 Stamnes (1994) documented the solutions for any even number of streams. The
365 computational efficiency of these models is lower than that of two-stream models while
366 their accuracy is better. To quantify the accuracy of the three two-stream algorithms for
367 snow shortwave simulations, we use the 16-stream DIScrete-Odinate Radiative Transfer
368 model (DISORT) as the benchmark model (http://lllab.phy.stevens.edu/disort/) (Stamnes
369 et al., 1988).

370

371 **3. Input for radiative transfer models**
372 In this work, we focus on the performance of two-stream algorithms for pure snow
373 simulations. The inputs for these three models are the same: single-scattering properties
374 (SSPs, i.e. single-scattering albedo ϖ, asymmetry factor g, extinction coefficient σ_{ext}) of
375 snow determined by snow grain radius r, snow depth, solar zenith angle θ, solar incident
376 flux, and the albedo of underlying ground (assuming Lambertian reflectance of 0.25 for
377 all wavelengths). A Delta-transform is applied to fundamental input optical variables for
378 all simulations (Equations 2 (a)-(c), Wiscombe and Warren, 1980).

379

380 In snow, photon scattering occurs at the air-ice interface, and the absorption of photons
381 occurs within the ice crystal. The most important factor that determines snow shortwave
382 properties is the ratio of total surface area to total mass of snow grains, aka "the specific
383 surface area" (e.g. Matzl and Schneebeli, 2006, 2010). The specific surface area (β) can
384 be converted to a radiatively effective snow grain radius r:

385

386 $\beta = 3 / (r \, \varrho_{ice})$ (10)

387

Author
Deleted: The algorithms used in

Author
Deleted: Icepack

Author
Deleted: speed

Author
Deleted: slower

10

where ρ_{ice} is the density of pure ice, 917 kg m^{-3}. Assuming the grains are spherical, the SSPs of snow can thus be computed using Mie theory (Wiscombe, 1980) and ice optical constants (Warren and Brandt, 2008). In nature, snow grains are not spherical, and many studies have been carried out to quantify the accuracy of such spherical representations (Grenfell and Warren, 1999; Neshyba et al., 2003; Grenfell et al., 2005). In recent years, more research has been done to evaluate the impact of grain shape on snow shortwave properties (Dang et al., 2016; He et al., 2017, 2018ab), and they show that non-spherical snow grain shapes mainly alter the asymmetry factor. Dang et al., (2016) also point out that the solar properties of a snowpack consisting of non-spherical ice grains can be mimicked by a snowpack consisting of spherical grains with a smaller grain size by factors up to 2.4. In this work, we still assume the snow grains are spherical, and this assumption does not qualitatively alter our evaluation of the radiative transfer algorithms.

The input SSPs of snow grains are computed using Mie theory at a fine spectral resolution for a wide range of ice effective radius r from 10 to 3000 μm that covers the possible range of grain radius for snow on Earth (Flanner et al., 2007). The same spectral SSPs were also used to derive the band-averaged SSPs of snow used in SNICAR. Note Briegleb and Light (2007) refer to SSPs as inherent optical properties.

4. Solar spectra used for the spectral integrations

In climate modeling, snow albedo computation at a fine spectral resolution is expensive and unnecessary. Instead of computing spectrally resolved snow albedo as shown in Figure 1, wider-band solar properties are more practical. For example, CESM and E3SM aggregate the narrow RRTMG bands used for the atmospheric radiative transfer simulation into visible (0.2 - 0.7 μm) and near-IR (0.7 - 5 μm) bands. The land model and sea-ice model thus receive visible and near-IR fluxes as the upper boundary condition, and return the corresponding visible and near-IR albedos to atmosphere model. In practice, these bands are also partitioned into direct and diffuse components. Therefore, a practical two-stream algorithm should be able to simulate the direct visible, diffuse visible, direct near-IR and diffuse near-IR albedos and absorptions of snow accurately.

The band albedo α is an irradiance-weighted average of the spectral albedo $\alpha(\lambda)$:

$$\alpha = \frac{\int_{\lambda_1}^{\lambda_2} \alpha(\lambda) F(\lambda) d\lambda}{\int_{\lambda_1}^{\lambda_2} F(\lambda) d\lambda} \qquad (11)$$

In this work, we use the spectral irradiance $F(\lambda)$ generated by the atmospheric DISORT-based Shortwave Narrowband Model (SWNB2) (Zender et al., 1997; Zender, 1999) for typical clear-sky and cloudy-sky conditions of mid-latitude winter as shown in Figure 2(a). The total clear-sky down-welling surface flux at different solar zenith angles are also given in Figure 2(b).

5. Model Evaluation

5.1 Spectral albedo and reflected solar flux

The spectral reflectance of pure deep snow computed using two-stream models and 16-stream DISORT are shown in Figure 1. The snow grain radius is 100 μm - a typical grain size for fresh new snow. For clear sky with direct beam source (left column), all three two-stream models show good accuracy at visible wavelengths (0.3 – 0.7 μm), and within this band, the snow albedo is large and close to 1. As wavelength increases, the albedo diminishes in the near-IR band. two-stream models overestimate snow albedo at these wavelengths, with maximum biases of 0.013 (SNICAR and dEdd-AD) and 0.023 (2SD) within wavelength 1 - 1.7 μm. For cloudy-sky cases with diffuse upper boundary conditions, dEdd-AD reproduces the snow albedo at all wavelengths with the smallest absolute error (< 0.005), SNICAR and 2SD both overestimate the snow albedo with maximum biases > 0.04 between 1.1-1.4 μm.

In both sky conditions, the errors of snow albedo are larger at near-IR wavelengths ranging from 1.0-1.7 μm, while the solar incident flux peaks at 0.5 μm then decrease as wavelength increases. The largest error in reflected flux is within the 0.7-1.5 μm band for SNICAR and 2SD, as shown in the 3rd row of Figure 1. dEdd-AD overestimate the direct snow albedo mostly at wavelengths larger than 1.5 μm where the error in reflected flux is almost negligible.

5.2 Broadband albedo and reflected solar flux

Integrated over the visible and near-IR wavelengths, the error in band albedos computed using two-stream models for different cases are shown in Figure 3-6.

Figure 3 shows the error in direct band albedo for fixed snow grain radius of 100 μm with different snow depth and solar zenith angles. As introduced in Section 2, SNICAR and dEdd-AD both use delta-Eddington method to compute the visible albedo. They overestimate the visible albedo for solar zenith angles smaller than 50° by up to 0.005,

12

Author
Deleted: Figure 2

Author
Deleted: CICE

Author
Deleted: CICE

Author
Deleted: s

Author
Deleted: Figure 2

Author
Deleted: CICE

Author
Deleted: CICE

and underestimate it for solar zenith angles larger than 50° by up to -0.01. 2SD produces similar results for the visible band but at a larger solar zenith angle threshold of 75°. In the near-IR band, SNICAR and 2SD overestimate the snow albedo for solar zenith angles smaller than 70°, beyond this, the error in albedo increases by up to -0.1 as solar zenith angle increases. dEdd-AD produces a similar error pattern with a smaller solar zenith angle threshold at 60°. As snow ages, its average grain size increases. For typical old melting snow of grain radius 1000 μm (Figure 4), two-stream models produce similar errors of direct albedo in all bands. For snow consisting of smaller grain size, two-stream models produce larger errors for visible albedo. Integrating over the entire solar band, the three two-stream models evaluated show similar error patterns for direct albedo.

For a fixed solar zenith angle of 60°, the error of direct albedo for different snow depth and snow grain radii are shown in Figure 5. SNICAR and dEdd-AD underestimate the visible albedo in most scenarios, while 2SD overestimates the visible albedo for a larger range of grain radius and snow depth. All three two-stream models tend to overestimate the near-IR albedo except for shallow snow with large grain radius; the error of 2SD is one order of magnitude larger than that of SNICAR and dEdd-AD.

Figure 6 is similar to Figure 5, but shows the diffuse snow albedo. In the visible band, SNICAR and dEdd-AD generate similar errors in that they both underestimate the albedo as snow grain size increases and snow depth decreases. 2SD overestimates the albedo with a maximum error of around 0.015. In the near-IR, two-stream models tend to overestimate snow albedo, while the magnitude of biases produced by SNICAR and 2SD are one order larger than that of dEdd-AD with the maximum error of 0.035 generated by SNICAR. As a result, the all-wave diffuse albedos computed using dEdd-AD are more accurate than those computed using SNICAR and 2SD.

Figures 7, 8 and 9 show the errors in reflected shortwave flux caused by snow albedo errors seen in Figures 3, 4, and 6. In general, two-stream models produce larger errors in reflected direct near-IR flux (Figure 7 and 8), especially with the 2SD model: the maximum overestimate of reflected near-IR flux is 6-8 Wm^{-2} for deep melting snow with solar zenith angle < 30°. Errors in reflected direct visible flux are smaller (mostly within ±1 Wm^{-2}) for all models in most scenarios, and become larger (mostly within ±3 Wm^{-2}) as snow grain size increases to 1000 μm if computed using 2SD. As shown in Figure 9, for diffuse flux with solar zenith angle of 60° at TOA, SNICAR and dEdd-AD generate

13

Author
Deleted: CICE

Author
Deleted: CICE

Author
Deleted: CICE

Author
Deleted: CICE

Author
Deleted: CICE

Author
Deleted: CICE

Author
Deleted: CICE

Author
Deleted: CICE

small errors in reflected visible flux (mostly within ±1 Wm^{-2}), while 2SD always overestimates reflected visible flux by up to 5 Wm^{-2}. In the near-IR, SNICAR and 2SD overestimate reflected flux by as much as 10-12 Wm^{-2}; the error in reflected near-IR flux produced by dEdd-AD is much smaller, mostly within ±1 Wm^{-2}.

In general, dEdd-AD produces the most accurate albedo and thus reflected flux for both direct and diffuse components. SNICAR is similar to dEdd-AD for its accuracy of direct albedo and flux, yet generates large error for the diffuse component. 2SD tends to overestimate snow albedo and reflected flux in both direct and diffuse components and shows the largest errors among three two-stream models. These relatively small differences between algorithms may still yield large impact on snowpack. For example, compared to dEdd-AD, SNICAR and 2SD overestimate the diffuse albedo by ~0.015 for melting snow (Figure 6). In Greenland, the daily averaged downward diffuse solar flux from May to September is 200 W/m^2, and the averaged cloud cover fraction is 80% (Figure 6, Dang et al., 2017). In this case, SNICAR and 2SD overestimate the reflected solar flux by 2.4 W/m^2 per day – the amount of energy otherwise enough to melt 10 cm of snow water equivalent from May to September. dEdd-AD also remediates self-compensating spectral biases (where visible and Near-IR biases are of opposite signs) present in the other schemes. Those spectral biases do not affect the broadband fluxes like the diffuse biases, but they nevertheless degrade proper feedbacks between snow/ice reflectance and heating."

5.3 Band absorption of solar flux

Figure 10 shows absorption profiles of shortwave flux computed using the 16-stream DISORT model, with errors in absorbed fractional solar flux computed using two-stream models. The snowpack is 10-cm deep and is divided into 5 layers, each 2-cm thick. The snow grain radius is set to 100 μm. The figure shows fractional absorption for snow layers 1-4 and the underlying ground with an albedo of 0.25.

As shown in the first column of Figure 10, for new snow with a radius of 100 μm, most solar absorption occurs in the top 2-cm snow layer, where roughly 10% and 15% of diffuse and direct near-IR flux are absorbed and dominate the solar absorption within the snowpack. In the second layer (2-4 cm), the absorption of solar flux is less than 1% and gradually decreases within the interior layers. The underlying ground absorbs roughly 2% of solar flux, mostly visible flux that penetrates the snowpack more efficiently. As snow

14

Author
Deleted: CICE

Author
Deleted: CICE

Author
Deleted: CICE

Author
Deleted: Note that the final errors of snow albedo and reflected solar flux are the weighted sum of direct and diffuse components, and their weights are largely determined by cloud cover fraction (e.g. Figure 6, Dang et al., 2017), which we do not address explicitly in this paper.

Author
Deleted: ,

Author
Deleted:

ages and snow grain grows, photons penetrate deeper into the snowpack. For typical old melting snow with a radius of 1000 μm, most solar absorption still occurs in the top 2-cm snow layer, where roughly 20% and 14% of diffuse and direct near-IR flux are absorbed. The second snow layer (2-4 cm) absorbs more near-IR solar flux by roughly 2%. More photons can penetrate through the snowpack, and results in a high fractionally absorption by the underlying ground, especially for the visible band. As snow depth increase, the ground absorption will decrease for both snow radii.

Comparing to 16-stream DISORT, two-stream models underestimate (overestimate) the column solar absorptions for new (old) snow, especially for the surface snow layer and the underground. Overall, dEdd-AD gives the most accurate absorption profiles among the three two-stream models, especially for new snow.

6. Correction for direct albedo for large solar zenith angles

It has been pointed out in previous studies that the two-stream approximations become poor as solar zenith angle approaches 90° (e.g. Wiscombe 1977, Warren 1982). As shown in Figures 3 and 4, all three two-stream models underestimate the direct snow albedo for large solar zenith angles. In the visible band, when the snow grain size is small, the error in direct albedo is almost negligible (Figure 3); while as snow ages and snow grains become larger, the error increases yet remains low if the snow is deep (Figure 4). In the near-IR, the biases of albedo are also larger for larger snow grain radii. For a given snow size, the magnitudes of such biases are almost independent of snow depth, and mainly determined by the solar zenith angle. In general, the errors of all-wave direct albedo are mostly contributed by the errors of near-IR albedo, especially for optically thick snowpacks (i.e., semi-infinite), because the errors of direct albedo in the visible are negligible compared with those in the near-IR. To improve the performance of two-stream algorithms, we develop a parameterization that corrects the underestimated near-IR snow albedo at large zenith angles.

Figure 11 shows the direct near-IR albedo and fractional absorption of 2-meter thick snowpacks consisting of grains with radius 100 μm and 1000 μm, computed using two-stream algorithms and 16-stream DISORT. For solar zenith angles > 75°, two-stream models underestimate snow albedo and overestimate solar absorption within snowpack, mostly in the top 2-cm of snow, and the differences among three two-stream models are small. In Section 5, we have shown that dEdd-AD produces the most accurate snow

15

albedo in general, with anticipated wide application of dEdd-AD, we develop the following parameterization to adjust its low biases in computed near-IR direct albedo.

We define and compute R_{75+} as the ratio of direct semi-infinite near-IR albedo computed using 16-stream DISORT ($\alpha_{16\text{-}DISORT}$) to that computed using dEdd-AD ($\alpha_{dEdd\text{-}AD}$). This ratio is shown in Figure 11 (c) and can be parameterized as a function of snow grain radius (r, unit in meter) and the cosine of incident solar zenith angle (μ_0), as shown in Figure 11(c):

$$R_{75+} = \frac{\alpha_{16-DISORT}}{\alpha_{dEdd-AD}} = c_1(\mu_0)log_{10}(r) + c_0(\mu_0) \tag{12}$$

where coefficients c_1 and c_0 are polynomial functions of μ_0, as shown in Figure 11(d):

$$c_1(\mu_0) = 1.304\mu_0^2 - 0.631\mu_0 + 0.086 \tag{13a}$$
$$c_0(\mu_0) = 6.807\mu_0^2 - 3.338\mu_0 + 1.467 \tag{13b}$$

Since two-stream models always underestimate snow albedo, R_{75+} always exceeds 1 (Figure 11c). We can then adjust the direct near-IR snow albedo ($\alpha_{dEdd\text{-}AD}$) and direct near-IR solar absorption ($Fabs_{dEdd\text{-}AD}$) by snow computed using dEdd-AD with ratio R_{75+}:

$$\alpha_{dEdd-AD}^{adjust} = R_{75+}\alpha_{dEdd-AD} \tag{14a}$$

$$Fabs_{dEdd-AD}^{adjust} = Fabs_{dEdd-AD} - (R_{75+} - 1)\alpha_{dEdd-AD}F_{nir} \tag{14b}$$

where F_{nir} is the direct near-IR flux. This adjustment reduces the error of near-IR albedo from negative 2-10% to within ± 0.5% for solar zenith angles larger than 75°, and for grain radii ranging from 30-1500 μm (Figure 12). Errors in broadband direct albedo are therefore also reduced to < 0.01. The direct near-IR flux absorbed by the snowpack decreases after applying this adjustment.

When the solar zenith angle exceeds 75°, our model adjusts the computed direct near-IR albedo αdEdd-AD by the ratio $R75+$, following equations 12-14a and reduces direct near-

IR absorption following equation 14b. If snow is divided into multiple layers, we assume all decreased near-IR absorption (2nd term on the right-hand side, equation 14b) is confined within the top layer. This assumption is fairly accurate for the near-IR band, since most absorption occurs at the surface of snowpack (Figures 10 and 11). As discussed previously, this parameterization is developed based on albedo computed using dEdd-AD. For models that do not use dEdd-AD but SNICAR and 2SD, the same adjustment still applies given the small differences of near-IR direct albedo computed using two-stream models (Figure 11). For models that adopt other radiative transfer algorithms it is best for the developers to examine their model against a benchmark model such as 16-stream DISORT or two-stream models discussed in this work before applying this correction.

It is important to note that although the errors of direct near-IR albedos are large for large solar zenith angles, the absolute error in reflected shortwave flux is small (Figures 7 and 8) as the down-welling solar flux reaches snowpack decreases as solar zenith angle increases (Figures 1(b)). However, such small biases in flux can be important to high latitudes where the solar zenith angle remains large for many days in late winter and early spring.

7. Implementation of snow radiative transfer model in Earth system models

ESMs often use broader band-averaged SSPs of snow and aerosols for computational efficiency, rather than using brute-force integration of spectral solar properties across narrower bands (per equation 11). Besides using different radiative transfer approximations, SNICAR and dEdd-AD also adopt different methods to derive the band-averaged SSPs of snow for different band schemes.

In SNICAR, snow solar properties are computed for 5 bands: one visible band (0.3 - 0.7μm), and four near-IR bands (0.7 - 1 μm, 1 – 1.2 μm, 1.2 – 1.5 μm, and 1.5 – 5 μm). The solar properties of four subdivided near-IR bands are combined by fixed ratios to compute the direct/diffuse near-IR snow properties. These two sets of ratios are derived offline based on the incident solar spectra of typical of mid-latitude winter for clear and cloudy-sky conditions clear sky and cloudy sky, respectively (Figure 1(a)).

The band-averaged SSPs of snow grains are computed following the Chandrasekhar Mean approach (Thomas and Stamnes, 1999, their Equation 9.27; Flanner et al., 2007).

17

702 Specifically, spectral SSPs of snow grains are weighted into bands according to surface
703 incident solar flux typical of mid-latitude winter for clear and cloudy sky conditions. In
704 addition, the single-scattering albedo $\varpi(\lambda)$ of ice grains are also weighted by the
705 hemispheric albedo $\alpha(\lambda)$ of an optically thick snowpack:
706

707 $$\varpi(\bar{\lambda}) = \frac{\int_{\lambda_1}^{\lambda_2} \varpi(\lambda)F(\lambda)\alpha(\lambda)d\lambda}{\int_{\lambda_1}^{\lambda_2} F(\lambda)\alpha(\lambda)d\lambda} \qquad (15a)$$

708 $$g(\bar{\lambda}) = \frac{\int_{\lambda_1}^{\lambda_2} g(\lambda)F(\lambda)d\lambda}{\int_{\lambda_1}^{\lambda_2} F(\lambda)\alpha(\lambda)d\lambda} \qquad (15b)$$

709 $$\sigma_{ext}(\bar{\lambda}) = \frac{\int_{\lambda_1}^{\lambda_2} \sigma_{ext}(\lambda)F(\lambda)d\lambda}{\int_{\lambda_1}^{\lambda_2} F(\lambda)\alpha(\lambda)d\lambda} \qquad (15c)$$

710

711 Two sets of snow band-averaged SSPs are generated for all grain radii, suitable for direct
712 and diffuse light, respectively. For each modeling step and band, SNICAR is called twice
713 to compute the direct and diffuse snow solar properties.
714

715 In dEdd-AD, the snow-covered sea ice properties are computed for 3 bands: one visible
716 band (0.3 – 07 µm), and two near-IR bands (0.7 – 1.19 µm and 1.19 – 5 µm). The solar
717 proprieties of these two near-IR bands are combined using ratios w_{nir1} and w_{nir2} for 0.7-1
718 .19 µm and 1.19-5 µm, depending on the fraction of direct near-IR flux f_{nidr}:
719

720 $$w_{nir1} = 0.67 + 0.11 * (1 - f_{nidr}) \qquad (16a)$$
721 $$w_{nir2} = 1 - w_{nir1} \qquad (16b)$$
722

723 The band SSPs of snow are derived by integrating the spectral SSPs and the spectral
724 surface solar irradiance measured in the Arctic under mostly clear sky.
725

726 $$\varpi(\bar{\lambda}) = \int_{\lambda_1}^{\lambda_2} \varpi(\lambda)F(\lambda)d\lambda \qquad (17a)$$

727 $$g(\bar{\lambda}) = \int_{\lambda_1}^{\lambda_2} g(\lambda)F(\lambda)d\lambda \qquad (17b)$$

728 $$\sigma_{ext}(\bar{\lambda}) = \int_{\lambda_1}^{\lambda_2} \sigma_{ext}(\lambda)F(\lambda)d\lambda \qquad (17c)$$

729

Author
Deleted: CICE

731 In addition, the band-averaged single-scattering albedo $\varpi(\bar{\lambda})$ is also increased to $\varpi(\bar{\lambda})'$

732 until the band albedo computed using averaged SSPs matches the band albedo $\bar{\alpha}$ within

733 0.0001, where $\bar{\alpha}$ is:

734

735 $$\bar{\alpha} = \int_{\lambda_1}^{\lambda_2} \alpha(\lambda)F(\lambda)d\lambda \qquad (18)$$

736

737 dEdd-AD adopts this single set of band SSPs for both direct and diffuse computations. In

738 practice, the physical snow grain radius r is adjusted to a radiatively equivalent radius r_{eqv}

739 based on the fraction of direct flux in the near-IR band (f_{nidr}):

740

741 $$r_{eqv} = (f_{nidr} + 0.8(1 - f_{nidr}))r \qquad (19)$$

742

743 This r_{eqv} and the corresponding snow SSPs are then used in the radiative transfer

744 calculation. The computed direct and diffuse solar properties alone are less accurate,

745 while the combined all-sky broadband solar properties agree with SNICAR (Briegleb and

746 Light, 2007). As a result, for each modeling step and band, dEdd-AD radiative transfer

747 subroutine is called only once to compute both the direct and diffuse snow solar

748 properties simultaneously.

749

750 SNICAR and dEdd-AD also use different approaches to avoid numerical singularities. In

751 SNICAR, singularities occur when the denominator of term $C_n^{\pm}$ in equation (3) equals to

752 zero (i.e., $\gamma^2 - 1/\mu_0^2 = 0$), where γ is determined by the approximation method and SSPs

753 of snow, and μ_0 is the cosine of the solar zenith angle (Equations 23 and 24, Toon et al.,

754 1989). When such a singularity is detected, SNICAR will shift μ_0 by + 0.02 or -0.02 to

755 obtain physically realistic radiative properties. In the dEdd-AD algorithm, singularities

756 arise only when $\mu_0 = 0$ (Equation 4). Therefore, in practice, for $\mu_0 < 0.01$, dEdd-AD

757 computes the sea-ice solar properties for $\mu_0 = 0.01$ to avoid unphysical results.

758

759 **8. Discussion: a unified radiative transfer model for snow, sea ice, and land ice.**

760
761
762 Based on the inter-comparison of three two-stream algorithms and their implementations

763 in ESMs, we formulated the following surface shortwave radiative transfer

Author
Deleted: CICE

Author
Deleted: CICE

Author
Deleted: CICE

Author
Deleted: CICE

Author
Deleted: CICE

769 recommendations for an accurate, fast, and consistent treatment for snow on land, land
770 ice, and sea ice in ESMs:

772 First, the two-stream delta-Eddington adding-doubling algorithm by Briegleb and Light
773 (2007) is unsurpassed as a radiative transfer core. The evaluation in Section 5 shows that
774 this algorithm produces the least error for snow albedo and solar absorption within
775 snowpack, especially under overcast skies. This algorithm applies well to both uniformly
776 refractive media such as snow on land, and to non-uniformly refractive media, such as
777 bare/snow-covered/ponded sea ice and bare/snow-covered land ice. Numerical
778 singularities occur only rarely (when $\mu_0 = 0$) and are easily avoided in model
779 implementations. Among the three two-stream algorithms discussed here, dEdd-AD is
780 also the most efficient one as it takes only ~2/3 of the time of SNICAR and 2SD to
781 compute solar properties of multi-layer snowpacks.

783 Second, any two-stream cryospheric radiative transfer model can incorporate the
784 parameterization described in Section 6 to adjust the low bias of direct near-IR snow
785 albedo and high bias of direct near-IR solar absorption in snow, for solar zenith angles
786 larger than 75°. These biases are persistent across all two-stream algorithms discussed in
787 this work, and should be corrected for snow-covered surfaces. Alternatively, adopting a
788 4-stream approximation would reduce or eliminate such biases, though at considerable
789 expense in computational efficiency.

791 Third, a cryospheric radiative transfer model should prefer physically based
792 parameterizations that are extensible and convergent (e.g., with increasing spectral
793 resolution) for the band-averaged SSPs and size distribution of snow. Although the
794 treatments used in SNICAR and dEdd-AD are both practical since they both reproduce
795 the narrowband solar properties with carefully derived band-averaged inputs as discussed
796 in Section 7, the snow treatment used in SNICAR is more physically based and
797 reproducible since it does not rely on subjective adjustment and empirical coefficients as
798 used in dEdd-AD. Specifically, the empirical adjustment to snow grain radius
799 implemented in dEdd-AD may not always produce compensating errors. For example, in
800 snow containing light-absorbing impurities such adjustment may also lead to biases in
801 aerosol absorption since the albedo reduction caused by light-absorbing particles does not
802 linearly depend on snow grain radius (Dang et al., 2015). For further model development
803 incorporating non-spherical snow grain shapes (Dang et al., 2016; He et al., 2018ab),
804 such adjustment on grain radius may fail as well. Moreover, SNICAR computes the snow

20

properties for four near-IR bands, which helps capture the spectral variation of albedo (Figure 1) and therefore better represents near-IR solar properties. It is also worth noting that unlike the radiative core of dEdd-AD, SNICAR is actively maintained with numerous modifications and updates in the past decade (e.g. Flanner et al., 2012; He et al., 2018b). Snow radiative treatments that follow SNICAR conventions for SSPs may take advantage of these updates. Note that any radiative core that follows SNICAR SSP conventions must be called twice to compute diffuse and direct solar properties, respectively.

Fourth, a surface cryospheric radiative transfer model should flexibly accommodate coupled simulations with distinct atmospheric and surface spectral grids. Both the 5-band scheme used in SNICAR and the 3-band scheme used in dEdd-AD separate the visible from near-IR spectrum at 0.7 µm. This boundary aligns with the Community Atmospheric Model's original radiation bands (CAM; Neale et al., 2012), though not with the widely used Rapid Radiative Transfer Model (RRTMG; Iacono et al., 2008) which places 0.7 µm squarely in the middle of a spectral band. A mismatch in spectral boundaries between atmospheric and surface radiative transfer schemes can require an ESM to unphysically apportion energy from the straddled spectral bin when coupling fluxes between surface and atmosphere. The spectral grids of surface and atmosphere radiation need not be identical so long as the coarser grid shares spectral boundaries with the finer grid. In practice maintaining a portable cryospheric radiative module such as SNICAR requires a complex offline toolchain (Mie solver, spectral refractive indices for air, water, ice, and aerosols, spectral solar insolation for clear and cloudy skies) to compute, integrate, and rebin SSPs. Aligned spectral boundaries between surface and atmospheric would simplify the development of efficient and accurate radiative transfer for the coupled Earth system.

Last, it is important to note that, although we only examine the performance of the dEdd-AD for pure snow in this work, this algorithm can be applied to the surface solar calculation of all cryospheric components with or without light-absorbing particles present. First, Briegleb and Light (2007) proved its accuracy for simulating ponded/bare sea-ice solar properties against observations and a Monte Carlo radiation model. Second, In CESM and E3SM, the radiative transfer simulation of snow on land ice is carried out by SNICAR with prescribed land ice albedo. Adopting dEdd-AD radiative core in SNICAR will permit these ESMs to couple the snow and land ice as a non-uniformly refractive column for more accurate solar computations since bare/snow-covered/ponded

21

land ice is physically similar to bare/snow-covered/ponded sea ice, and the latter is already treated well by dEdd-AD radiative transfer core. Third, adding light-absorbing particles in snow will not change our results qualitatively. Both dEdd-AD and SNICAR simulate the impact of light-absorbing particles (black carbon and dust) on snow and/or sea ice using self-consistent particle SSPs that follow the SNICAR convention (e.g., Flanner et al., 2007; Holland et al. 2012). These particles are assumed to be either internally or externally mixed with snow crystals; the combined SSPs of mixtures (e.g. Appendix A of Dang et al., 2015) are then used as the inputs for radiative transfer calculation. The adoption of dEdd-AD radiative transfer algorithm in SNICAR, and the implementation of SNICAR snow SSPs in dEdd-AD enables a consistent simulation of the radiative effects of light-absorbing particles in the cryosphere across ESM components.

In summary, this inter-comparison and evaluation has shown multiple ways that the solar properties of cryospheric surfaces can be improved in the current generation of ESMs. We have merged these findings into a hybrid model SNICAR-AD, which is primarily composed of the radiative transfer scheme of dEdd-AD, 5-band snow/aerosol SSPs of SNICAR, and the parameterization to correct for snow albedo biases when solar zenith angle exceeds 75°. This hybrid model can be applied to snow on land, land ice, and sea ice to produce consistent shortwave radiative properties for snow-covered surfaces across the Earth system. With the evolving and further understanding of snow and aerosol physics and chemistry, the adoption of this hybrid model will obviate the effort to modify and maintain separate optical variable input files used for different model components.

SNICAR-AD is now implemented in both the sea-ice (MPAS-seaice) and land (ELM) components of E3SM. More simulations and analyses are underway to examine its impact on E3SM model performance and simulated climate. The results are however beyond the scope of this work and will be thoroughly discussed in a future paper.

9. Conclusions

In this work, we aim to improve and unify the solar radiative transfer calculations for snow on land and snow on sea ice in ESMs by evaluating the following two-stream radiative transfer algorithms: the two-stream delta-Eddington adding-doubling algorithm dEdd-AD implemented in sea-ice model Icepack/CICE/MPAS-seaice, the two-stream delta-Eddington and two-stream delta-Hemispheric-Mean algorithms implemented in snow model SNICAR, and a two-stream delta-Discrete-Ordinate algorithm. Among these three models, the dEdd-AD produces the most accurate snow albedo and solar absorption

22

(Section 5). All two-stream models underestimate near-IR snow albedo and overestimate near-IR absorption when solar zenith angles are larger than 75°, which can be adjusted by a parameterization we developed (Section 6). We compared the implementations of radiative transfer cores in SNICAR and dEdd-AD (Section 7) and recommended a consistent and hybrid shortwave radiative model SNICAR-AD for snow-covered surfaces across ESMs (Section 8). Improved treatment of surface cryospheric radiative properties in the thermal infrared has recently been shown to remediate significant climate simulation biases in Polar Regions (Huang et al., 2018). It is hoped that adoption of improved and consistent treatments of solar radiative properties for snow-covered surfaces as described in this study will further remediate simulation biases in snow-covered regions.

References

Aoki, T., Kuchiki, K., Niwano, M., Kodama, Y., Hosaka, M. and Tanaka, T.: Physically based snow albedo model for calculating broadband albedos and the solar heating profile in snowpack for general circulation models. Journal of Geophysical Research, 116, D11114, https://doi.org/10.1029/2010JD015507, 2011.

Bøggild, C.E., Brandt, R.E., Brown, K.J. and Warren, S.G.: The ablation zone in northeast Greenland: ice types, albedos and impurities. Journal of Glaciology, 56, 101-113, pp.101-113, https://doi.org/10.3189/002214310791190776, 2010.

Brandt, R.E., Warren, S.G., Worby, A.P. and Grenfell, T.C.: Surface albedo of the Antarctic sea ice zone. Journal of Climate, 18(17), pp.3606-3622. https://doi.org/10.1175/JCLI3489.1 2005.

Briegleb, P. and Light, B.: A Delta-Eddington mutiple scattering parameterization for solar radiation in the sea ice component of the community climate system model, 2007.

Dang, C. and Hegg, D.A.: Quantifying light absorption by organic carbon in Western North American snow by serial chemical extractions. Journal of Geophysical Research, 119(17), pp.10-247. https://doi.org/10.1002/2014JD022156, 2014.

Dang, C., Fu, Q. and Warren, S.G., 2016. Effect of snow grain shape on snow albedo. Journal of the Atmospheric Sciences, 73(9), pp.3573-3583. https://doi.org/10.1175/JAS-D-15-0276.1, 2016.

Dang, C., Brandt, R.E. and Warren, S.G.: Parameterizations for narrowband and broadband albedo of pure snow and snow containing mineral dust and black carbon. Journal of Geophysical Research: Atmospheres, 120(11), pp.5446-5468, https://doi.org/10.1002/2014JD022646, 2015.

Dang, C., Warren, S.G., Fu, Q., Doherty, S.J., Sturm, M. and Su, J.: Measurements of light-absorbing particles in snow across the Arctic, North America, and China: Effects on surface albedo. Journal of Geophysical Research: Atmospheres, 122(19), pp.10-149. https://doi.org/10.1002/2017JD027070, 2017.

972 Doherty, S.J., Hegg, D.A., Johnson, J.E., Quinn, P.K., Schwarz, J.P., Dang, C. and
973   Warren, S.G.: Causes of variability in light absorption by particles in snow at sites in
974   Idaho and Utah. Journal of Geophysical Research: Atmospheres, 121(9), pp.4751-
975   4768. https://doi.org/10.1002/2015JD024375, 2016.

976 Doherty, S.J., Warren, S.G., Grenfell, T.C., Clarke, A.D. and Brandt, R.E.: Light-
977   absorbing impurities in Arctic snow. Atmospheric Chemistry and Physics. 10(23),
978   pp.11647-11680. https://doi.org/10.5194/acp-10-11647-2010, 2010.

979 Doherty, S.J., Dang, C., Hegg, D.A., Zhang, R. and Warren, S.G.: Black carbon and other
980   light-absorbing particles in snow of central North America. Journal of Geophysical
981   Research: Atmospheres, 119(22), pp.12-807, https://doi.org/10.1002/2014JD022350,
982   2014.

983 Flanner, M.G. and Zender, C.S.: Snowpack radiative heating: Influence on Tibetan
984   Plateau climate. Geophysical Research Letters, 32(6).
985   https://doi.org/10.1029/2004GL022076, 2005.

986 Flanner, M.G., Zender, C.S., Randerson, J.T. and Rasch, P.J.: Present-day climate forcing
987   and response from black carbon in snow. Journal of Geophysical Research:
988   Atmospheres, 112(D11). https://doi.org/10.1029/2006JD008003, 2007.

989 Flanner, M.G., Liu, X., Zhou, C., Penner, J.E. and Jiao, C.: Enhanced solar energy
990   absorption by internally-mixed black carbon in snow grains. Atmospheric Chemistry
991   and Physics, 12(10), pp.4699-4721. https://doi.org/10.5194/acp-12-4699-2012, 2012.

992 Gardner, A.S. and Sharp, M.J.: A review of snow and ice albedo and the development of
993   a new physically based broadband albedo parameterization. Journal of Geophysical
994   Research: Earth Surface, 115(F1). https://doi.org/10.1029/2009JF001444, 2010.

995 Grenfell, T.C., Neshyba, S.P. and Warren, S.G.: Representation of a nonspherical ice
996   particle by a collection of independent spheres for scattering and absorption of
997   radiation: 3. Hollow columns and plates. Journal of Geophysical Research:
998   Atmospheres, 110(D17). https://doi.org/10.1029/2005JD005811, 2005.

999 He, C., Liou, K.N., Takano, Y., Yang, P., Qi, L. and Chen, F.: Impact of grain shape and
1000   multiple black carbon internal mixing on snow albedo: Parameterization and radiative
1001   effect analysis. Journal of Geophysical Research: Atmospheres, 123(2), pp.1253-
1002   1268. https://doi.org/10.1002/2017JD027752, 2018a.

1003 He, C., Flanner, M.G., Chen, F., Barlage, M., Liou, K.N., Kang, S., Ming, J. and Qian,
1004   Y.: Black carbon-induced snow albedo reduction over the Tibetan Plateau:
1005   uncertainties from snow grain shape and aerosol–snow mixing state based on an
1006   updated SNICAR model. Atmospheric Chemistry and Physics, 18, pp.11507-11527.
1007   https://doi.org/10.5194/acp-18-11507-2018, 2018b.

1008 He, C., Takano, Y., Liou, K.N., Yang, P., Li, Q. and Chen, F.: Impact of Snow Grain
1009   Shape and Black Carbon–Snow Internal Mixing on Snow Optical Properties:
1010   Parameterizations for Climate Models. Journal of Climate, 30(24), pp.10019-10036.
1011   https://doi.org/10.1175/JCLI-D-17-0300.1, 2017.

1012 Holland, M.M., Bailey, D.A., Briegleb, B.P., Light, B. and Hunke, E.: Improved sea ice
1013   shortwave radiation physics in CCSM4: The impact of melt ponds and aerosols on

Arctic sea ice. Journal of Climate, 25(5), pp.1413-1430. https://doi.org/10.1175/JCLI-
D-11-00078.1, 2012.

Huang, X., Chen, X., Flanner, M., Yang, P., Feldman, D. and Kuo, C.: Improved
representation of surface spectral emissivity in a global climate model and its impact
on simulated climate. Journal of Climate, 31(9), pp.3711-3727.
https://doi.org/10.1175/JCLI-D-17-0125.1, 2018.

Hunke, E. C., Lipscomb, W. H., Turner, A. K., Jeffery, N., and Elliott, S.: CICE: the Los
Alamos Sea Ice Model Documentation and Software User's Manual Version 4.1 LA-
CC-06-012. T-3 Fluid Dynamics Group, Los Alamos National Laboratory 675. 2010.

Iacono, M.J., Delamere, J.S., Mlawer, E.J., Shephard, M.W., Clough, S.A. and Collins,
W.D.: Radiative forcing by long-lived greenhouse gases: Calculations with the AER
radiative transfer models. Journal of Geophysical Research: Atmospheres, 113(D13),
https://doi.org/10.1029/2008JD009944, 2008.

Jin, Z. and Stamnes, K.: Radiative transfer in nonuniformly refracting layered media:
atmosphere–ocean system. Applied Optics, 33(3), pp.431-442.
https://doi.org/10.1364/AO.33.000431, 1994.

Kuipers Munneke, P., Van den Broeke, M.R., Lenaerts, J.T.M., Flanner, M.G., Gardner,
A.S. and Van de Berg, W.J.: A new albedo parameterization for use in climate
models over the Antarctic ice sheet. Journal of Geophysical Research: Atmospheres,
116(D5). https://doi.org/10.1029/2010JD015113, 2011.

Lee, W.L. and Liou, K.N.: A coupled atmosphere–ocean radiative transfer system using
the analytic four-stream approximation. Journal of the Atmospheric Sciences, 64(10),
pp.3681-3694. https://doi.org/10.1175/JAS4004.1, 2007.

Liang, S., Fang, H., Chen, M., Shuey, C.J., Walthall, C., Daughtry, C., Morisette, J.,
Schaaf, C. and Strahler, A.: Validating MODIS land surface reflectance and albedo
products: Methods and preliminary results. Remote sensing of environment, 83(1-2),
pp.149-162. https://doi.org/10.1016/S0034-4257(02)00092-5, 2002.

Light, B., Grenfell, T. C. and Perovich, D.K.: Transmission and absorption of solar
radiation by Arctic sea ice during the melt season. Journal of Geophysical Research:
Oceans 113, no. C3, https://doi.org/10.1029/2006JC003977, 2008.

Light, B., Perovich, D.K., Webster M.A., Polashenski, C., and Dadic, R.: Optical
properties of melting first-year Arctic sea ice. Journal of Geophysical Research:
Oceans 120, no. 11: 7657-7675, https://doi.org/10.1002/2015JC011163, 2015.

Marshall, S. and Oglesby, R.J.: An improved snow hydrology for GCMs. Part 1: Snow
cover fraction, albedo, grain size, and age. Climate Dynamics, 10(1-2), pp.21-37.
https://doi.org/10.1007/BF00210334, 1994.

Marshall, S.E.: A Physical Parameterization of Snow Albedo for Use in Climate Models,
NCAR Cooperative Thesis 123, National Center for Atmospheric Research,
Boulder, CO, 175 pp. 1989.

1053 Matzl, M. and Schneebeli, M.: Measuring specific surface area of snow by near-infrared
1054   photography. Journal of Glaciology, 52(179), pp.558-564.
1055   https://doi.org/10.3189/172756506781828412, 2006.

1056 Matzl, M. and Schneebeli, M.: Stereological measurement of the specific surface area of
1057   seasonal snow types: Comparison to other methods, and implications for mm-scale
1058   vertical profiling. Cold Regions Science and Technology, 64(1), pp.1-8.
1059   https://doi.org/10.1016/j.coldregions.2010.06.006, 2010.

1060 Meador, W.E. and Weaver, W.R.: Two-stream approximations to radiative transfer in
1061   planetary atmospheres: A unified description of existing methods and a new
1062   improvement. Journal of the Atmospheric Sciences, 37(3), pp.630-643.
1063   https://doi.org/10.1175/1520-0469(1980)037<0630:TSATRT>2.0.CO;2, 1980.

1064 Mlawer, E.J. and Clough, S.A.: On the extension of rapid radiative transfer model to the
1065   shortwave region. In Proceedings of the 6th Atmospheric Radiation Measurement
1066   (ARM) Science Team Meeting, US Department of Energy, CONF-9603149, 223–
1067   226. 1997.

1068 Neale, Richard B., Chen, C.-C., Gettelman, A., Lauritzen, P. H., Park, S., Williamson, D.
1069   L., Conley, A. J., Garcia, R., Kinnison, D., Lamarque, J. F., and Marsh, D.:
1070   Description of the NCAR community atmosphere model (CAM 5.0). NCAR Tech.
1071   Note NCAR/TN-486+ STR 1, no. 1: 1-12. 2010.

1072 Neshyba, S.P., Grenfell, T.C. and Warren, S.G.: Representation of a nonspherical ice
1073   particle by a collection of independent spheres for scattering and absorption of
1074   radiation: 2. Hexagonal columns and plates. Journal of Geophysical Research:
1075   Atmospheres, 108(D15). https://doi.org/10.1029/2002JD003302, 2003.

1076 Perovich, D. K.: The optical properties of sea ice (No. MONO-96-1). COLD REGIONS
1077   RESEARCH AND ENGINEERING LAB HANOVER NH. 1996.

1078 Stamnes, K., Tsay, S.C., Wiscombe, W. and Jayaweera, K.: Numerically stable algorithm
1079   for discrete-ordinate-method radiative transfer in multiple scattering and emitting
1080   layered media. Applied optics, 27(12), pp.2502-2509.
1081   https://doi.org/10.1364/AO.27.002502, 1988.

1082 Thomas, G.E. and K. Stamnes (1999), Radiative transfer in the atmosphere and ocean.
1083   Cambridge University Press.

1084 Toon, O. B., McKay, C. P., Ackerman, T. P., and Santhanam, K.: Rapid calculation of
1085   radiative heating rates and photodissociation rates in inhomogeneous multiple
1086   scattering atmospheres, J. Geophys. Res., 94(D13), 16,287–16,301.
1087   https://doi.org/10.1029/JD094iD13p16287, 1989.

1088 Turner, A.K., Lipscomb, W.H., Hunke, E.C., Jacobsen, D.W., Jeffery, N., Ringler, T.D.
1089   and Wolfe, J.D.: MPAS-Seaice: a new variable resolution sea-ice model. J. Adv.
1090   Model Earth Sy., in preparation., 2018.

1091 Wang, X., Doherty, S.J. and Huang, J.: Black carbon and other light-absorbing
1092   impurities in snow across Northern China. Journal of Geophysical Research:
1093   Atmospheres, 118(3), pp.1471-1492. https://doi.org/10.1029/2012JD018291, 2013.

1094   Warren, S. G.: Optical properties of snow. Reviews of Geophysics 20, no. 1: 67-89.
1095   https://doi.org/10.1029/RG020i001p00067,1982.

1096   Warren, S.G. and Wiscombe, W.J.: A model for the spectral albedo of snow. II: Snow
1097   containing atmospheric aerosols. Journal of the Atmospheric Sciences, 37(12),
1098   pp.2734-2745.https://doi.org/10.1175/1520-
1099   0469(1980)037<2734:AMFTSA>2.0.CO;2, 1980

1100   Warren, S.G. and Brandt, R.E.: Optical constants of ice from the ultraviolet to the
1101   microwave: A revised compilation. Journal of Geophysical Research: Atmospheres,
1102   113(D14). https://doi.org/10.1029/2007JD009744, 2008.

1103   Warren, S.G. and Wiscombe, W.J.: Dirty snow after nuclear war. Nature, 313(6002),
1104   p.467. https://doi.org/10.1038/313467a0, 1985.

1105   Wiscombe, W. J.: The delta-Eddington approximation for a vertically inhomogeneous
1106   atmosphere, NCAR Tech. Note TN-140_STR [NTIS P6270618]. 1977.

1107   Wiscombe, W.J.: Improved Mie scattering algorithms. Applied optics, 19(9), pp.1505-
1108   1509. https://doi.org/10.1364/AO.19.001505,1980.

1109   Wiscombe, W.J. and Warren, S.G.: A model for the spectral albedo of snow. I: Pure
1110   snow. Journal of the Atmospheric Sciences, 37(12), pp.2712-2733.
1111   https://doi.org/10.1175/1520-0469(1980)037<2712:AMFTSA>2.0.CO;2, 1980.

1112   Zender, C.S.: Global climatology of abundance and solar absorption of oxygen collision
1113   complexes. Journal of Geophysical Research: Atmospheres, 104(D20), pp.24471-
1114   24484. https://doi.org/10.1029/1999JD900797, 1999.

1115   Zender, C.S., Bush, B., Pope, S.K., Bucholtz, A., Collins, W.D., Kiehl, J.T., Valero, F.P.
1116   and Vitko Jr, J.: Atmospheric absorption during the atmospheric radiation
1117   measurement (ARM) enhanced shortwave experiment (ARESE). Journal of
1118   Geophysical Research: Atmospheres, 102(D25), pp.29901-29915.
1119   https://doi.org/10.1029/97JD01781, 1997.

1120

1121 The spectral albedo of pure snow computed using 16-stream DISORT,
1122 SNICAR, dEdd-AD, and 2SD models, for clear-sky (direct beam at solar zenith angle
1123 60°) and cloudy-sky conditions in the left and right panels, respectively. The top panels
1124 show spectral albedo. The middle panels show the difference ($\delta\alpha = \alpha_2 - \alpha_{16}$) in spectral
1125 albedos computed using the two-stream model (α_2) and 16-stream DISORT (α_{16}). The
1126 bottom panels show the difference of reflected spectral flux given $\delta\alpha$. The snowpack is
1127 set to semi-infinite deep with grain radius of 100 μm.
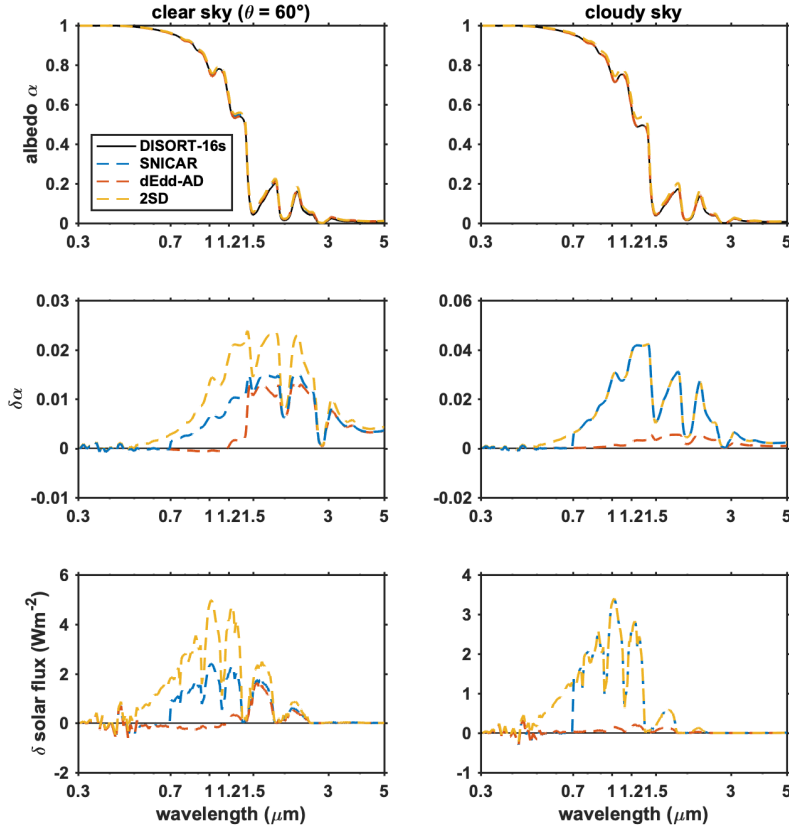
1128
1129
1130
1131

1133 Figure 2. Spectral and total down-welling solar flux at surface computed using SWNB2
1134 for (a) standard clear-sky and cloudy-sky atmospheric profiles of mid-latitude winter
1135 assuming solar zenith angle is 60° at the top of the atmosphere, and for (b) standard clear
1136 sky profiles of mid-latitude and sub-Arctic winter with different incident solar zenith
1137 angles.
1138
1139

1140
1141
1142

30
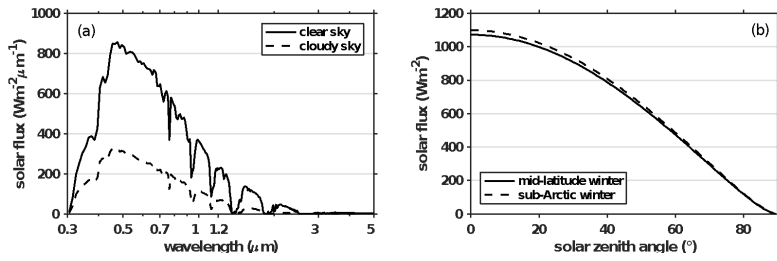
1143 Figure 3. The difference in direct snow albedo ($\delta\alpha = \alpha_s - \alpha_{io}$) computed using two-stream
1144 models (α_s) and using 16-stream DISORT model (α_{io}), for various snow depths and solar
1145 zenith angles, with snow grain radius of 100 μm. From the top to the bottom rows are
1146 results of two-stream models SNICAR, dEdd-AD, and 2SD. From the left to the right
1147 columns are albedo differences of all-wave, visible, near-IR bands.
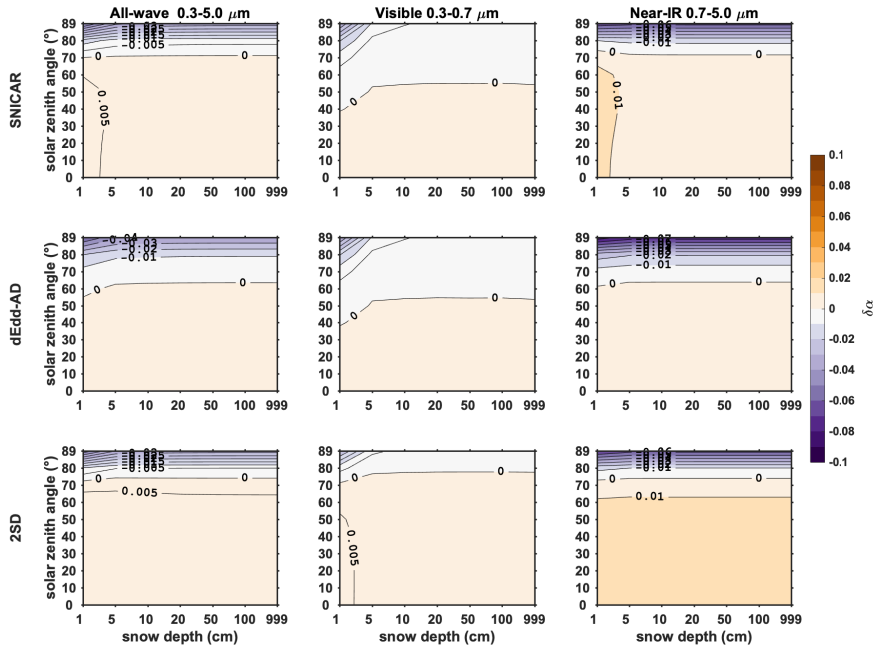
1148
1149
1150

1152 Figure 4. The difference in direct snow albedo ($\delta\alpha = \alpha_c - \alpha_{16}$) computed using two-stream
1153 models (α_c) and using 16-stream DISORT model (α_{16}) for various snow depths and solar
1154 zenith angles, with snow grain radius of 1000 μm.
1155
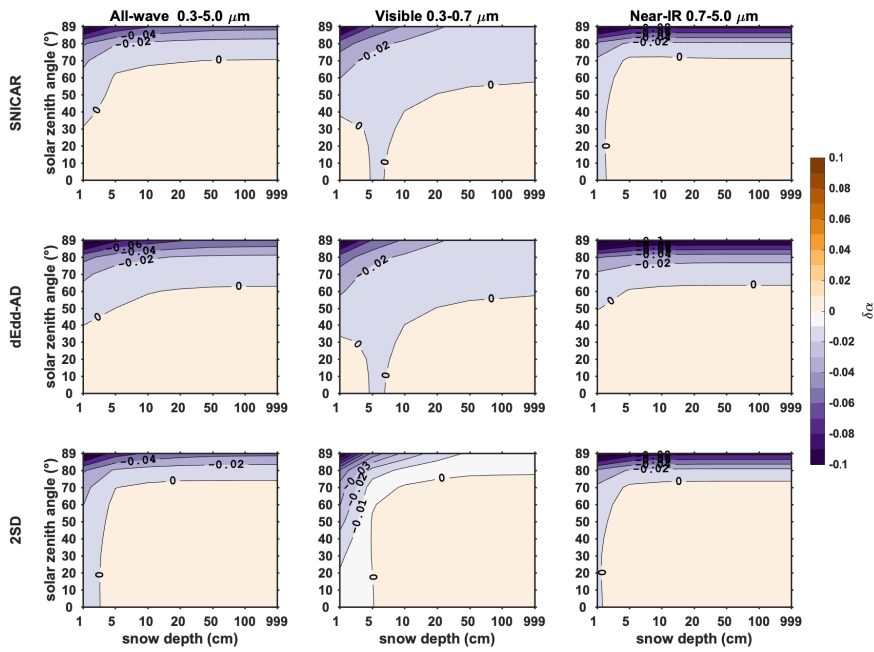
1156
1157
1158

Figure 5. The difference in direct snow albedo ($\delta\alpha = \alpha_2 - \alpha_{16}$) computed using two-stream models (α_2) and using 16-stream DISORT model (α_{16}), for various snow depths and snow grain radii, with solar zenith angle of 60°.
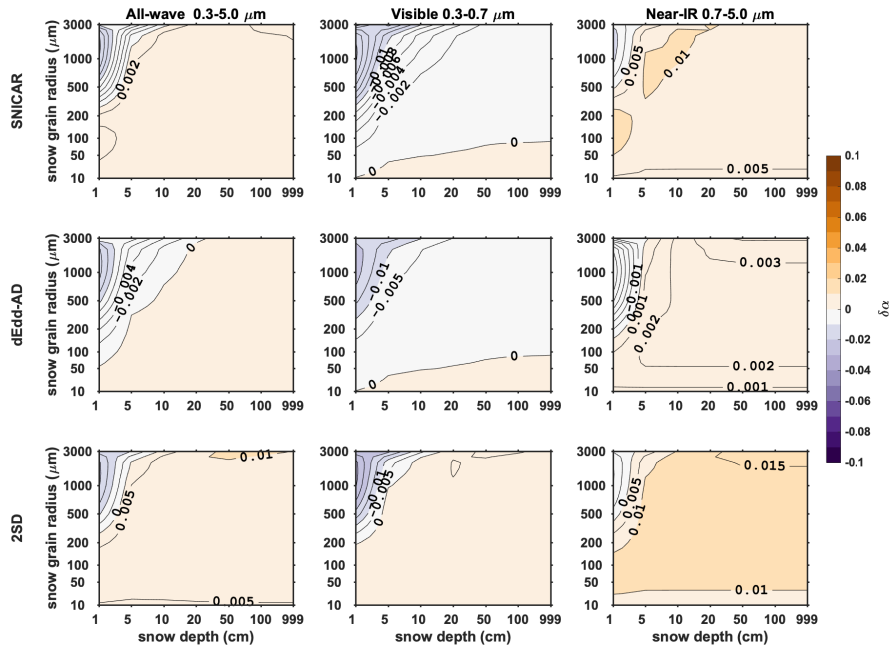
33

1169 Figure 6. The difference in diffuse snow albedo ($\delta\alpha = \alpha_2 - \alpha_{16}$) computed using two-
1170 stream models (α_2) and using 16-stream DISORT model (α_{16}), for various snow depths
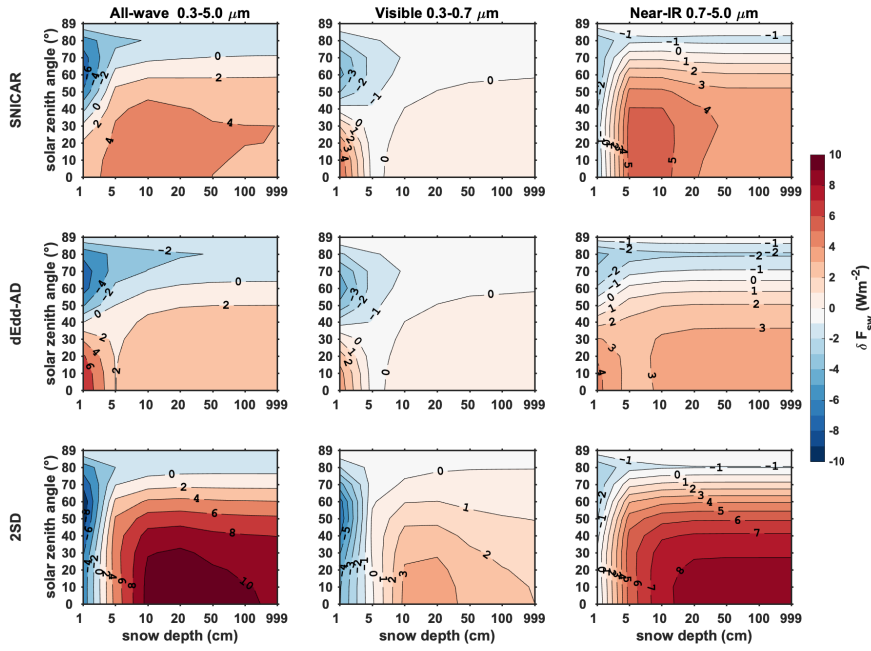1171 and snow grain radii, with solar zenith angle of 60° at the top of the atmosphere.
1172
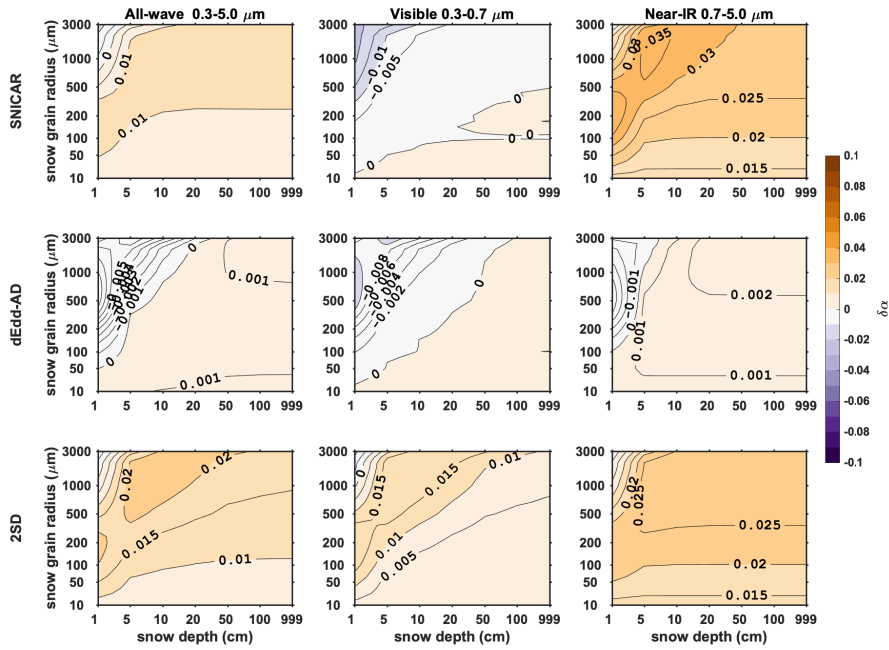
1173

34

1177   Figure 7. Error in reflected direct solar flux given albedo errors shown in Figure 3.
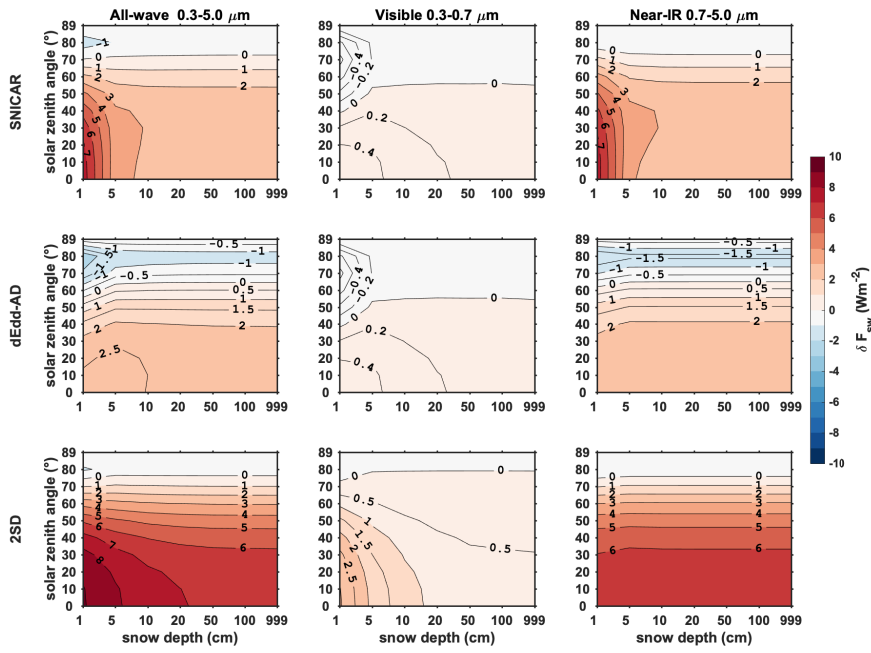
1178
1179

Figure 8. Error in reflected direct solar flux given albedo errors shown in Figure 4.

1184   Figure 9. Error in reflected diffuse solar flux given albedo errors shown in Figure 6.
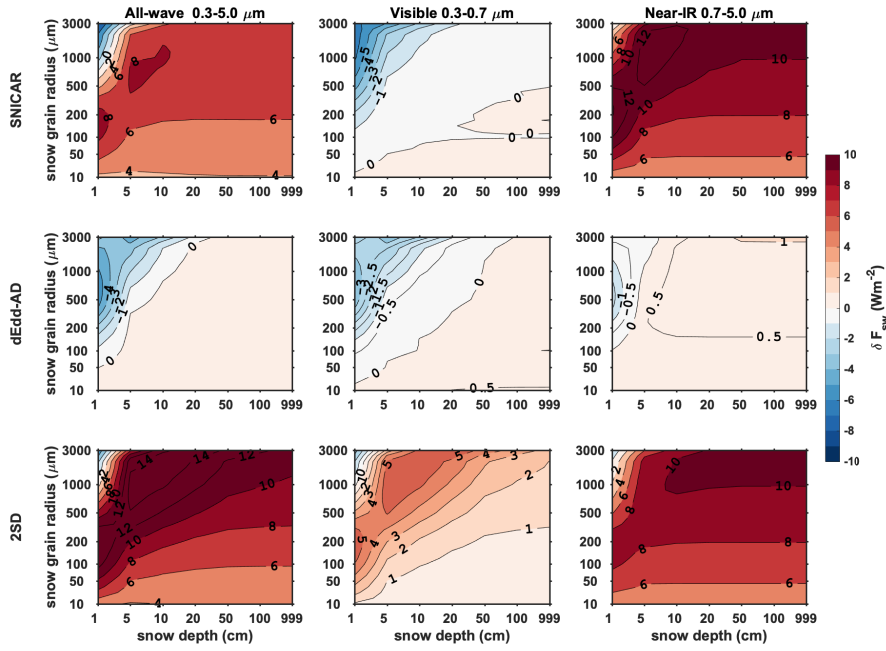
1185
1186
1187

Figure 10. Comparison of light-absorption profiles derived from two-stream models and 16-stream DISORT. The left-most column shows fractional band absorptions computed using 16-stream DISORT. The right three panels show the errors of all-wave, visible, and near-IR fractional absorptions calculated using two-stream models. The top and bottom panels are for clear-sky and cloudy-sky conditions (solar zenith angle of 60°), respectively. The snowpack is 10 cm deep and is divided evenly into five 2-cm thick layers, for new snow (r = 100 μm) and old snow (r = 1000 μm). The layers 1-4 represent the top four snow layers (top 8 cm), and layer 5 represents underlying ground with albedo of 0.25.
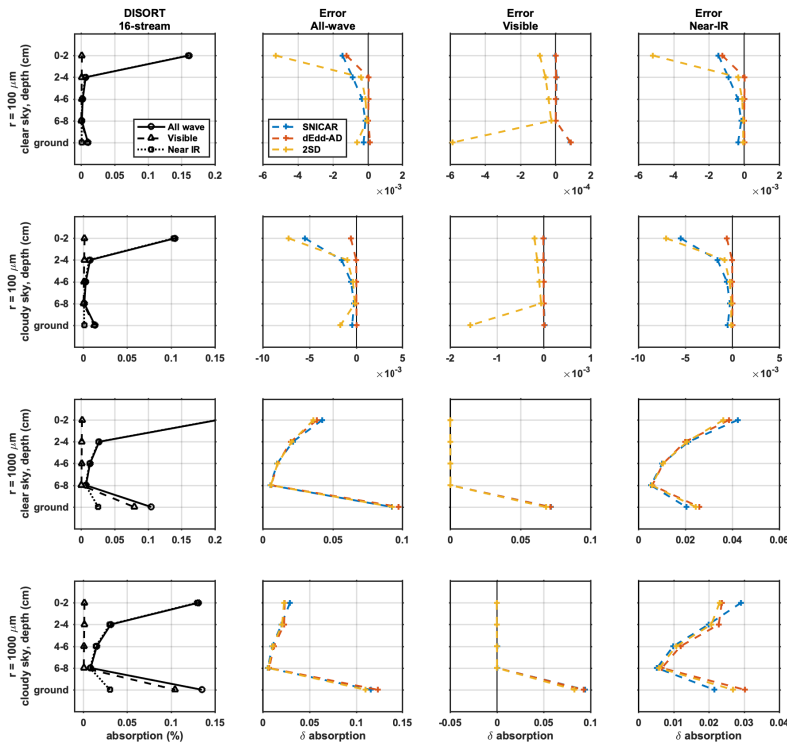
1200
1201 Figure 11. (a) Direct near-IR snow albedo and (b) near-IR fractional absorption by top 2-
1202 cm snow of a 2-m thick snowpack, for solar zenith angles larger than 70° and snow grain
1203 radii of 100 μm and 1000 μm. (c) The ratios of near-IR albedo computed using CICE to
1204 that computed using 16-stream DISORT for different solar zenith angles. These ratios are
1205 parameterized as linear functions of the logarithmic of snow grain radius. The slopes and
1206 y-intercepts are shown in (d). The black dashed curves in figures (c) and (d) are fitting
1207 values computed using parameterization discussed in Section 5.
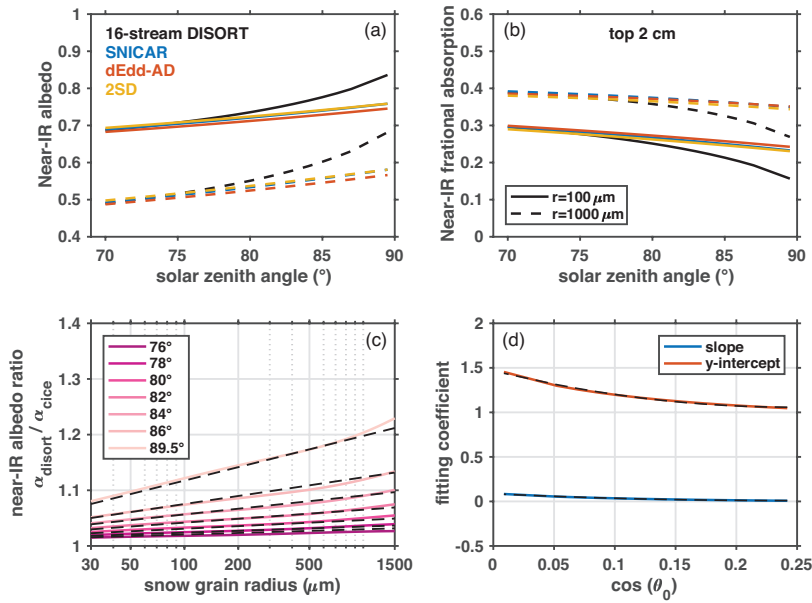
1208
1209
1210
1211

1212 Figure 12. Error in semi-infinite snow albedo computed using dEdd-AD, before (top row)
1213 and after (bottom row) incorporating corrections for near-IR albedo, for different solar
1214 zenith angles and snow grain radii.
1215
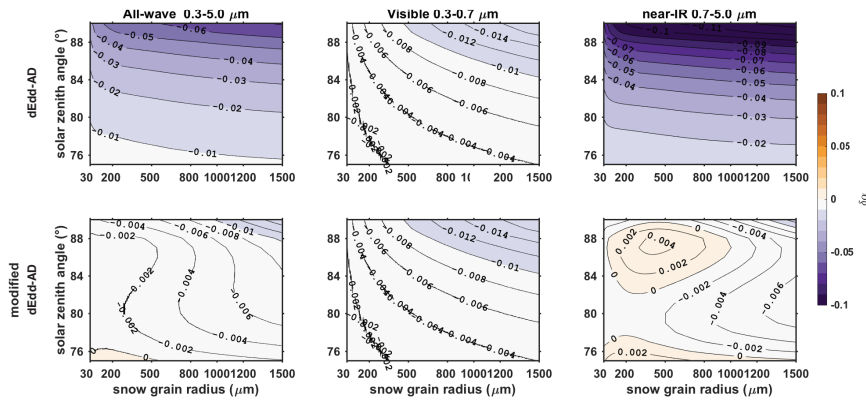
1216
1217
1218
1219

1221 Table 1. Acronyms used in this paper and their references.
1222
1223

ESM/ESMs	Earth System Models	
E3SM	Energy Exscale Earth System Model	Global climate model, previously know as ACME, https://e3sm.org/
CESM	Community Earth System Model	Global climate model, http://www.cesm.ucar.edu/
CCSM	Community Climate System Model	Global climate model, http://www.cesm.ucar.edu/models/ccsm 4.0/
RACMO	Regional Atmospheric Climate Model	Regional model, https://www.projects.science.uu.nl/iceclimate/models/racmo.php
CAM	Community Atmospheric Model	Atmospheric model, Neale et al., 2012
ELM	E3SM land model	Land model of E3SM, https://e3sm.org/model/e3sm-model-description/v1-description/
CLM	Community land model	Land model of CESM, http://www.cesm.ucar.edu/models/clm/
MPAS-seaice	Model for Prediction Across Scales Sea Ice	Sea-ice model of E3SM, Turner et al., 2018
CICE	Los Almos Sea Ice Model	Sea-ice model of CESM, Hunke et al., 2010
RRTM	Rapid Radiative Transfer Model	Standalone column radiative transfer model, Mlawer and Clough, 1997, http://rtweb.aer.com/rrtm_frame.html
RRTMG	Rapid Radiative Transfer Model for GCM components	Modified RRTM for GCM application, Iacono et al., 2008, http://rtweb.aer.com/rrtm_frame.html
DISORT	DIScrete-Odinate Radiative Transfer model	Standalone column radiative transfer model, http://lllab.phy.stevens.edu/disort/, Stamnes et al., 1988
SWNB2	Shortwave Narrowband Model	Standalone column radiative transfer model, Zender et al., 1997; Zender, 1999
SNICAR	SNow ICe and Aerosol Radiative module	Snow module used in ELM and CLM, Flanner and Zender, 2005; Toon et al., 1989

dEdd-AD	Two-stream delta-Eddington Adding-Doubling radiative transfer algorithm	Sea-ice radiative transfer core in MPAS-seaice and CICE, Briegleb and Light, 2007
2SD	Two-Stream Discrete ordinate radiative transfer algorithm	Radiative transfer algorithm tested in this work, Jin and Stamnes, 1994
SNICAR-AD	SNICAR – Adding Doubling	Hybrid snow/sea-ice radiative transfer model, Section 8
SSP/SSPs	Single-Scattering Properties	Single-scattering albedo ϖ, asymmetry factor g, extinction coefficient σ_{ext}
near-IR	Near Infrared band	Wavelengths of 0.7 - 5 μm

1224
1225

1226
1227 Table 2. Two-stream radiative transfer algorithms evaluated in this work, including
1228 algorithms that are currently implemented in Earth System Model CESM and E3SM.
1229
1230

ESM Component	Land	Sea Ice	
Model	SNICAR	dEdd-AD	2SD
Radiative transfer approximation	two-stream δ-Eddington (visible) δ-Hemispheric-mean (near-IR)	two-stream δ-Eddington	two-stream δ-Discrete-ordinate
Treatment for multi-layered media	matrix inversion	adding-doubling	matrix inversion
Fresnel reflection/refraction	no	yes	yes
Number of bands implemented in ESMs	5 bands (1 visible, 4 near-IR)	3 bands (1 visible, 2 near-IR)	
Applies to	snow	bare/ponded/snow-covered sea ice, and snow	bare/ponded/snow-covered sea ice, and snow

1231